Applied Physics Express

LETTER • **OPEN ACCESS**

Low-frequency multiplex CARS microscopy with a high-repetition near-infrared supercontinuum laser

OPEN ACCESS

Applied Physics Express 14, 122006 (2021) LETTER

https://doi.org/10.35848/1882-0786/ac39b1

Low-frequency multiplex CARS microscopy with a high-repetition near-infrared supercontinuum laser

Yusuke Arashida[1], Atsushi Taninaka[1,2], Takahiro Ochiai[1,2], Hiroyuki Mogi[1], Shoji Yoshida[1], Masamichi Yoshimura[3], Osamu Takeuchi[1], and Hidemi Shigekawa[1*]

[1]Faculty of Pure and Applied Sciences, University of Tsukuba, Tsukuba 305-8573, Japan
[2]TAKANO Co., Ltd., Miyada-mura, Kamiina-gMiyada-muraun, Nagano, 399-4301, Japan
[3]Graduate School of Engineering, Toyota Technological Institute, Hisakata, Tempaku, Nagoya 468-8511, Japan

*E-mail: hidemi @ims.tsukuba.ac.jp

Received October 28, 2021; revised November 12, 2021; accepted November 15, 2021; published online November 25, 2021

We have developed a multiplex coherent anti-Stokes Raman scattering microscope effective for low-wavenumber measurement by combining a high-repetition supercontinuum light source of 1064 nm and a near-infrared high-sensitivity InGaAs diode array. This system could observe the low-wavenumber region down to 55 cm^{-1} with high sensitivity. In addition, using spectrum shaping and spectrum modulation techniques, we simultaneously realized a wide bandwidth (<1800 cm^{-1}), high wavenumber resolution (9 cm^{-1}), high efficiency, and increasing signal-to-noise ratio by reducing the effect of the background shape in the low-wavenumber region. Spatial variation of a sulfur crystal phase transition with metastable states was visualized. © 2021 The Author(s). Published on behalf of The Japan Society of Applied Physics by IOP Publishing Ltd

Supplementary material for this article is available online

The chemical information obtained by Raman scattering is actively used in various fields such as bioscience, physical chemistry, material science, and structural mechanics.[1–6] In particular, Raman scattering has been widely applied to bioimaging microscopes by taking advantage of its noncontact, minimally invasive, and label-free characteristics.[7] Measurement efficiency has been markedly improved by stimulated Raman spectroscopy and coherent anti-Stokes Raman spectroscopy (CARS), which utilize pulsed laser technology.[8–12] A wide bandwidth, high-frequency resolution, and high throughput were realized simultaneously by a multiplex CARS method that utilized spectrum shaping technology.[13–16]

In Raman spectroscopy, the main cause of damage is the thermal process caused by light absorption, which is a factor that makes analysis by Raman spectroscopy difficult. In addition, although the efficiency is significantly improved by measurement methods such as CARS, since Raman spectroscopy measures weak signals, light other than Raman scattered light such as fluorescence affects the measurement. Since many materials fluoresce in the ultraviolet–visible region, it is necessary to use light with a longer wavelength than the ultraviolet–visible region to reduce the fluorescence.

However, a high-sensitivity Si image sensor, which is widely used for observing visible light, has a significantly reduced sensitivity to light with a wavelength of 1 μm or more, corresponding to a wavenumber of about 600 cm^{-1} or less. In such a low-frequency region, important information such as structure of compounds containing relatively heavy atoms such as P, S, and Fe as well as hydrates and polymers, appears.[17–21] Therefore, the development of a new technology is strongly required.

In this study, we have developed a multiplex CARS microscope that is effective for low-wavenumber measurement by combining a high-repetition infrared supercontinuum (SC) laser and an infrared high-sensitivity diode array. A high efficiency, wide bandwidth, high wavenumber resolution, and low background were simultaneously realized.

Figure 1 shows the outline of the developed multiplex CARS microscopy system. The excitation was carried out by a SC light source (FIU15, NKT Photonics) obtained by passing the output of a mode-locked laser (center wavelength: 1064 nm, pulse duration: 5 ps) through a highly nonlinear fiber (HNF, FIU-15). The wavelength range is 400–2400 nm, the repetition frequency f_{rep} is variable ($f_{rep} = 78/n$ MHz, $n = 1$ to 40), and the maximum pulse energy is 78 nJ. Visible light components were removed in advance with a long-pass filter (LPF: FELH1050, Thorlabs). The SC light was divided into transmitted light (angular frequency of ω_s) and reflected light (ω_p) by an ultrasteep LPF (ULPF1: LP02-1064RU-25, Semlock). At this time, the linewidth was narrowed by passing the ω_p-light through a bandpass filter (BPF: 1064.2-0.6, Alluxa) with a full width at half maximum (FWHM) of 0.7 nm. The two beams were combined by the ULPF1 after adjusting the optical path length. By transmitting the combined light through ULPF2 (LP01-1064-RE, Semlock), the light with wavelengths shorter than 1058 nm was blocked. The obtained light was focused on a sample using an objective lens (LCPLN100XIR, Olympus) with NA = 0.85 installed in an inverted optical microscope (IX83, Olympus).

The light reflected from the sample was collected by the same objective lens (epi-detection) and separated from the laser light by reflecting it on ULPF2. The obtained signal was measured with a spectroscope (SpetraPro 2300i, Princeton Instruments, grating of 600 grooves mm^{-1}) and a nitrogen-cooled InGaAs photodiode array (PyLoN-IR-1024-1.7). As will be described later, a resolution of 9.6 cm^{-1} was obtained. The quantum efficiency is 0.2 or less in the visible light region, but a high quantum efficiency (>0.8) is possible at wavelengths of 950 nm or more.

The CARS process is a third-order nonlinear optical process generated by irradiating light of ω_p and ω_s, as shown in Fig. 1(b). The vibration mode Ω_i of the sample is excited by the difference in frequency between ω_p and ω_s and the anti-Stokes line whose frequency is shifted by Ω_i from ω_p is

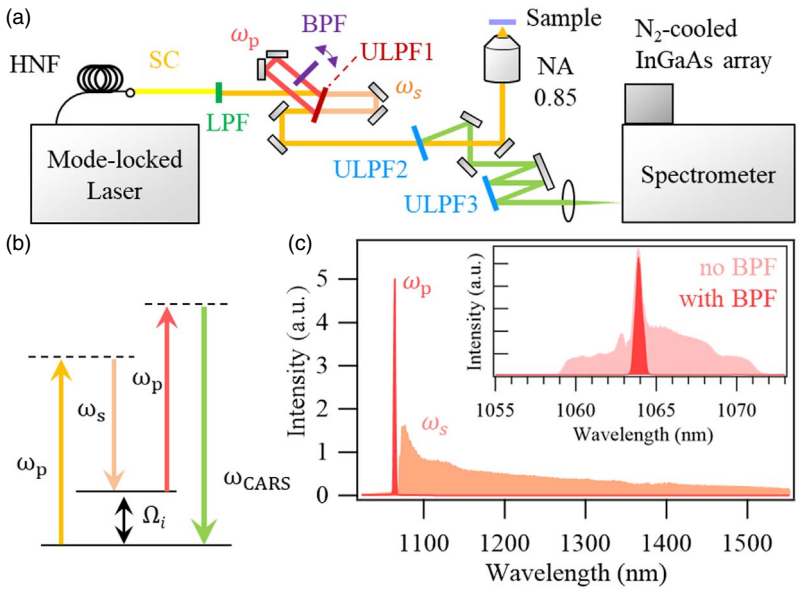

Fig. 1. (Color online) Developed system and analysis method. (a) Setup of the infrared low-frequency multiplex CARS system using a supercontinuum laser. HNF: highly nonlinear fiber, (U)LPF: (ultrasteep) long-pass filter, and BPF: bandpass filter. The light spot position was controlled by the *XY* stage (Nano-BioS200, MCL Inc.) on which the sample was placed. Spot sizes of ω_p, ω_s and the spatial resolution are shown in Figs. S4 and S5 (supporting information). Since the laser beam could not be completely removed by one reflection, it was reflected twice more by ULPF3. This part can be simplified if a short-pass filter with a narrow edge width near 1064 nm is used. (b) Energy diagram of CARS. Ω_i: frequency of a vibration mode. (c) The spectrum of the laser incident on the sample. Inset: spectra of ω_p around 1064 nm with (red) and without (light red) the BPF.

measured. As shown in Fig. 1(c), the spectrum at the sample position is a combination of the narrow-linewidth beam ω_p and the wideband beam ω_s. An enlarged view of the spectrum of ω_p is shown in the inset. To improve the spectral resolution, a part of the spectrum of ω_p with a finite width is narrowed using a BPF with a linewidth of 0.7 nm (FWHM).

CARS measurement generally produces broad light with the same frequency as the signal. This is called non-resonant background (NRB), and it occurs strongly, especially in the low-frequency region. Previous studies have attempted to improve the signal-to-noise (SN) ratio by utilizing the interference between the CARS signal and NRB;[12] a notch was made in the broad spectrum and ω_{CARS} was extracted from the difference between the two spectra, which was measured by slightly changing the wavelength of the notch. In our study, ω_{CARS} was obtained by taking the difference between the two spectra measured by changing the wavelength of ω_p by $\delta\omega$ using a BPF and a rotation stage (ELL18K/M, Thorlabs). The advantage of modulating the peak-type ω_p frequency is that the SN can be improved because the intensity of ω_p can be increased compared with the case of using a notch described above.

However, in this method, attention must be paid to the spectral shape caused by the interference between CARS and NRB. Assuming that the complex electric fields generated by CARS and NRB are E_{CARS} and E_{NR}, respectively, the frequency dependence of the detected light intensity can be expressed

$$I(\omega) = |E_{CARS} + E_{NR}|^2 = |E_{CARS}|^2 + |E_{NR}|^2 + 2\,\mathrm{Re}[E_{NR}^* E_{CARS}]. \quad (1)$$

The third term on the right side is produced by interference. When E_{CARS} has a resonance peak shape and E_{NR} is a non-phase-sensitive background, the spectrum with the Fano shape appears when the NRB amplitude is sufficiently larger than the CARS signal [see Fig. S1(a) available online at stacks.iop.org/APEX/14/122006/mmedia]. On the other hand, when the effect of interference by NRB is small, a spectrum with a peak appears {see Fig. S1(b)}. Then, when the difference between the two spectra obtained by changing ω_p is considered, the spectrum has a structure with the largest slope at the frequency Ω_i. To obtain an accurate Raman shift, it is necessary to consider fitting with the degree of interference.

First, the bandwidth of the IR excitation multiplex CARS microscope was evaluated. A polyimide film with a thickness of 12.5 μm was used as a sample. Polyimide is a polymer in which aromatic compounds are linked via an imide bond and has high thermal, mechanical, and chemical stabilities. However, polyimide exhibits strong fluorescence over the entire visible light range.[22] Therefore, when Raman measurement is performed with a visible light source, processing is necessary to reduce the background.[22] Numerous vibrational modes derived from the polyimide structure were observed in a wide band from 586 to 1788 cm^{-1} (see Fig. S2). The attribution of each peak according to previous studies[23–25] is as described in the caption of Fig. S2. The upper limit of 1800 cm^{-1} is due to the negative dispersion of the broadband Stokes light (see Fig. S3).

Next, low-wavenumber CARS spectra and removal of NRB is discussed. A sulfur crystal was used as a sample, whose structures at room temperature and pressure are known to be α-S_8 (pale yellow orthorhombic), β-S_8 (pale yellow monoclinic), and γ-S_8 (pale yellow needle-shaped monoclinic). All have a cyclic octamer ring S_8 as a unit structure, the α-type is the most stable at 95.6 °C or lower, and the β-type is the most stable above 95.6 °C. In this experiment,

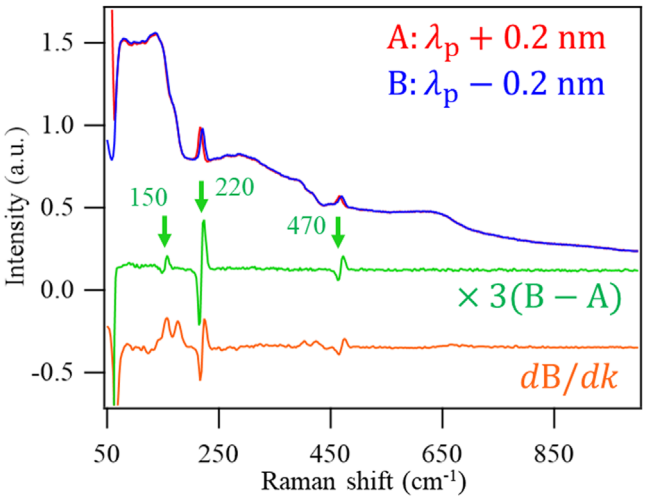

Fig. 2. (Color online) CARS spectra obtained for the sulfur crystal at room temperature. Red and blue curves are raw spectra (top lines) obtained at room temperature with slightly different wavelengths of λ_p. Exposure time was 100 ms with the laser power of 24.0 mW at the sample. The green curve is the difference between the red and blue spectra (middle line). The orange curve is the numerical derivative of the blue spectrum (bottom line) with respect to the Raman shift k. dA/dk showed the same shape in the region larger than 100 cm^{-1} (not shown here).

the sample was sandwiched between a gold mirror (PF10-03-M03, Thorlabs) and a sapphire substrate (thickness of 0.1 mm).

The blue line in Fig. 2 shows the spectrum obtained from the sample at room temperature. Sharp peaks of 220 cm^{-1} and 470 cm^{-1} were observed in the broad spectrum. The red line overlapping the blue line shows the spectrum obtained by changing λ_p by 0.4 nm by changing the angle of the BPF. To distinguish the CARS signal from the NRB, we took the difference between the red and blue spectra and obtained the green spectrum. Three CARS peaks can be seen in the spectrum. From the high-frequency side, 470 cm^{-1} is the signal originating from the S–S bond stretching of the S_8 bond structure, 220 cm^{-1} is the signal from the symmetric S–S bending (called the 220 cm^{-1} peak hereafter), and 150 cm^{-1} is the signal from the asymmetric S–S bending.[17] All three peaks were hardly affected by interference and had a shape similar to that shown in Fig. S1(b). However, since the NRB spectrum changes sharply at the peak position of 150 cm^{-1}, it is essential to confirm the existence of this peak in the difference spectrum.

For comparison, the orange line shows the result of numerically differentiating the raw data. Multiple peaks appeared in addition to the CARS signal, which is due to the complex shape of the background at $<650\,cm^{-1}$, as shown in the raw data (top lines) in Fig. 2. Moreover, since such NRB shape strongly depends on materials, the evaluation of signals becomes complicated. In contrast, obtaining a signal by taking the difference of two data can effectively reduce such a problem. Namely, it was confirmed that the method of obtaining the spectrum using the BPF is especially effective in distinguishing the CARS signal in the low-wavenumber region where the effect of NRB is relatively large and characteristic. The wavenumber resolution of the developed system was 9.6 cm^{-1} (FWHM), and the lower limit of the measurement on the low-wavenumber side was 55 cm^{-1}, which is the lowest value obtained thus far by multiplex CARS using IR light with a wavelength of 1064 nm or longer.

Next, we confirmed the high efficiency of the developed system. By IR excitation multiplex CARS, we achieved the same high measurement efficiency as that in previous research using visible light excitation, even on the low-wavenumber side of the fingerprint region.[17] Besides, IR excitation could induce CARS while suppressing the sample damages caused by light irradiation, as expected (see Fig. S5).

Then, the change in the intensity and shift of the Raman signal accompanying the phase transition of a sulfur crystal was observed. The sample was heated to 120 °C to liquefy it, then it was naturally cooled to solidify it, and the changes during the process were probed. Figure 3(a) shows the CARS difference spectra when the temperature was increased from room temperature to 120 °C, obtained as shown in Fig. 2, with each spectrum normalized by the peak height of 470 cm^{-1}. Almost the same spectral shape was observed from room temperature to 90 °C, but the intensity of the 220 cm^{-1} peak decreased at 95 °C. It is considered that the sample underwent a phase transition to a monoclinic structure at 95 °C. The sample was liquefied at 105 °C, and the spectral shape did not change further at higher temperatures. Since the eight-membered ring is stable up to 160 °C, three peaks derived from S_8 were observed even for the liquid.

Subsequently, Fig. 3(b) shows the results of observation while cooling the sample from 120 °C. The spectrum of the liquid phase did not change until 60 °C below the melting point of 105 °C. Since the wavelength of the 220 cm^{-1} peak shifted to the higher-frequency side by 3.5 cm^{-1}, it is considered that the sample solidified at 60 °C, a temperature lower than the conventional melting point, because of the supercooling effect.

Figure 3(c) shows an enlarged view of the Raman spectra obtained before (blue), at 95 °C; during heating (orange), for the liquid (red), and at 60 °C; during cooling (green). The peak position did not change significantly between the initial temperature and 95 °C; however, its shift to the low-wavenumber side was observed in the liquid phase. During re-solidification, it shifted to the higher-wavenumber side than that in the initial state.

Figure 3(d) shows the temperature dependence of the magnification of the shift shown in Fig. 3(c). The values on the vertical axis were obtained by fitting the spectra in Figs. 3(a) and 3(b). For the fitting function, the sum of two Lorentz functions with slightly different center positions and opposite signs was used. The peak position, which was initially at 222 cm^{-1}, gradually decreased with heating and rapidly changed to 220 cm^{-1} at the liquefaction temperature of 105 °C. When the sample was cooled after reaching 120 °C, there was no significant change at 105 °C owing to the effect of the supercooling. After the gradual shift to the high-frequency side, a sudden change in peak position from about 220.2–223.4 cm^{-1} occurred at 62 °C. The reason why the wavenumber was different from that in the initial state is considered to be the generation of a γ-type phase instead of the initial α-type phase.[17] The slight decrease in frequency when the β-type is generated is considered to be due to the increase in the relative intensity of the lower-frequency side in the double peak structure of the mode reported in the

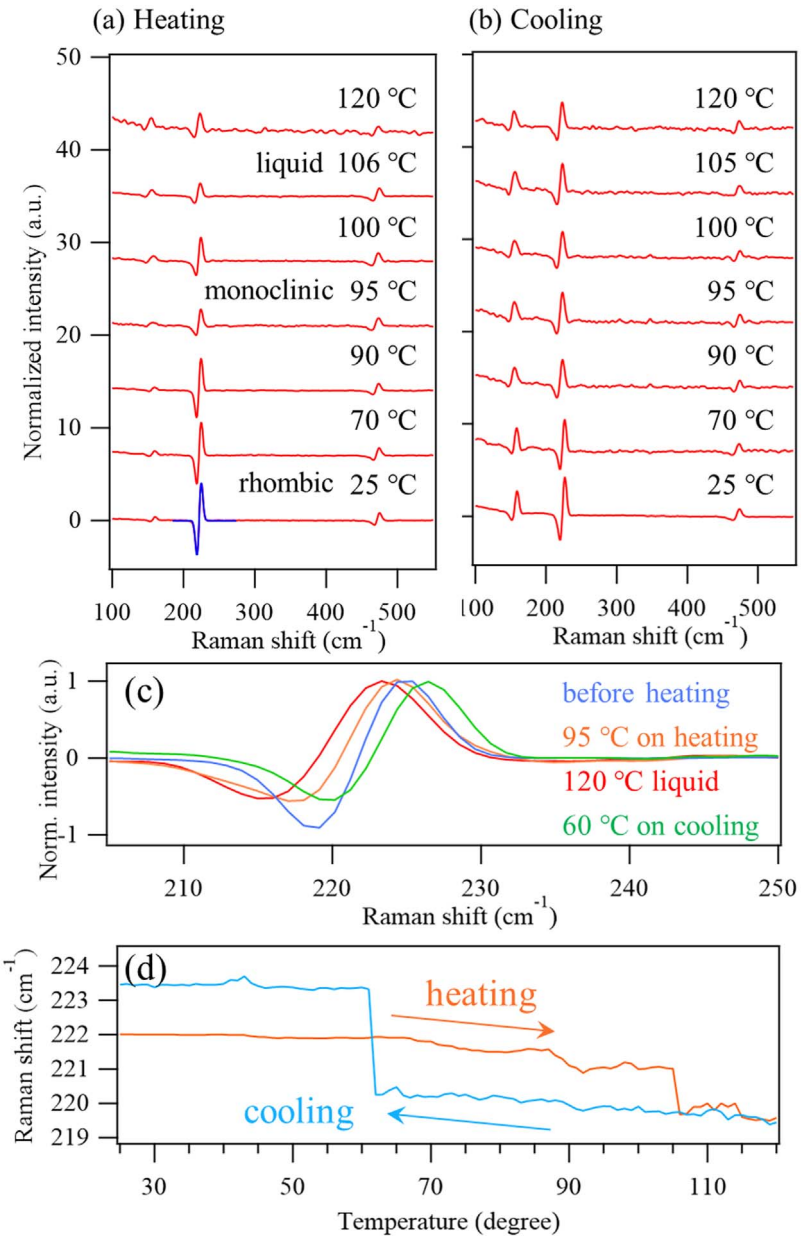

Fig. 3. (Color online) Spectra obtained for the phase transition of a Sulfur crystal. Dependence of the substrate temperature of the difference spectra obtained as shown in Fig. 2 with (a) increasing and (b) decreasing the substrate temperature. All spectra were normalized by the height of the 470 cm^{-1} peak. (c) Raman spectra obtained before heating (blue), 95 °C during heating (orange), for the liquid (red), and at 60 °C during cooling (green). (d) Temperature dependence of the Raman shift of the peak near 220 cm^{-1} (called the 220 cm^{-1} peak hereafter) obtained by fitting the data in (a) and (b). When the fitting was performed with Lorentzian and Gaussian functions, the degree of shape matching depended on the temperature, but the peak position was the same for both. At 25 °C in (a), fitting by the Lorentzian function is overlapped. The rate of heating and cooling is ~1.5 °C min^{-1}. The accuracy of the temperature is <0.2 °C for each spectrum.

high-resolution measurement.[17] The change in the peak intensity of 150 cm^{-1} appeared slightly different from that of 220 cm^{-1} when the temperature was increased. However, the temperature dependence of the peak shift and the temperature at which the intensity change occurred were similar for both peaks. In addition, the association with each phase was consistent with the previous study.[17] The analysis of the Raman spectrum thus clarified the details of the spectral change due to the phase transition of a sulfur crystal during heating and cooling.

Next, we visualized the phase transition. CARS spectra were measured over a 50 × 50 μm^2 area (100 × 100 points) at different temperatures, and the results are shown in Fig. 4. The temperature was increased from room temperature to 120 °C and then returned to room temperature. Figure 4(a) shows the mapping of the 1064 nm scattered light intensity I_0 at different temperatures. The optical contrast affected by the shape, refractive index, and thickness of the sample was visualized. Some differences were observed in the images between 25 °C and 80 °C during heating and between 60 °C and 25 °C during cooling, despite the temperatures being lower than the phase transition temperature. Namely, gradual changes appear to occur in the crystal structure. At 95 °C during cooling, the sample was in a liquid phase owing to the effect of the supercooling, so a non-uniform distribution appeared in the scattered light intensity. This is considered to represent the effect of the substrate on multiple reflections.

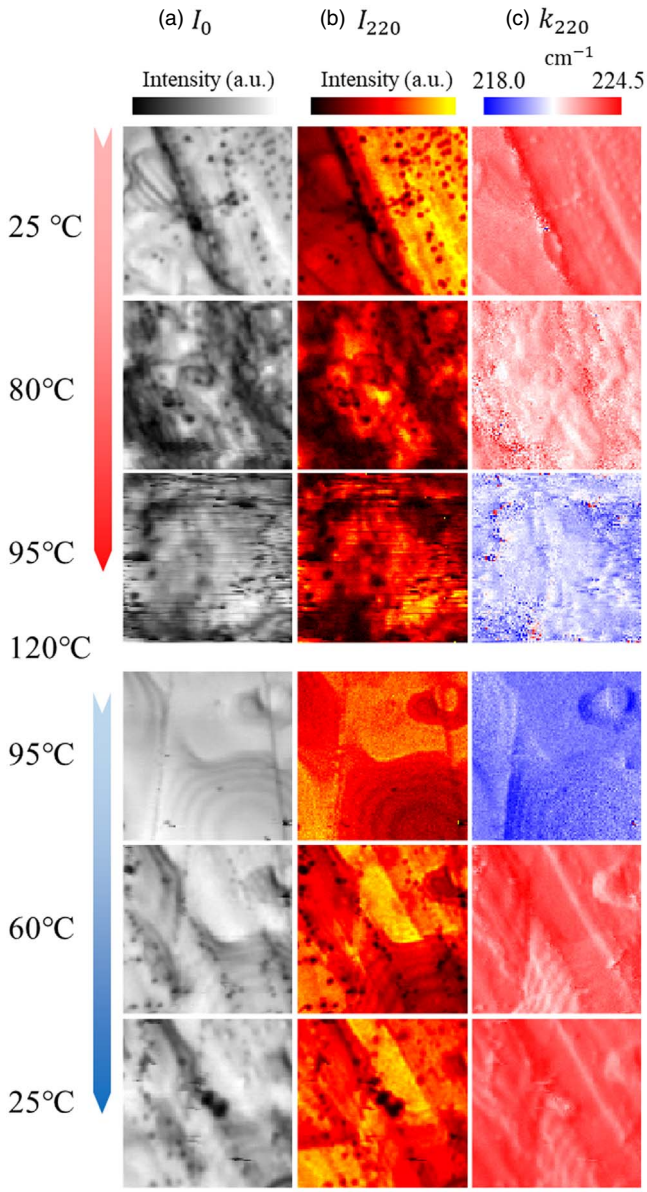

Fig. 4. (Color online) Visualization of the phase transition. The spatial distributions of (a) the intensity of the scattered light of 1064 nm, I_o, (b) the intensity of the CARS signal of the 220 cm^{-1} peak, I_{220}, and (c) the magnitude of the Raman shift of the 220 cm^{-1} peak are shown. k_{220} is the central wavenumber of the 220 cm^{-1} peak. The full scale of all images is 50 μm × 50 μm, and measurements were performed at 100 × 100 points. It took 0.7 s to obtain two spectra at each point by changing the wavelength of ω_p by $\delta\omega$ using the BPF and the rotation stage, as shown in Fig. 1, which can be shortened about one order with a Galvano system.

The strength of the signal in the 220 cm^{-1} peak, I_{220}, is mapped in Fig. 4(b). The intensity distribution was different from that of the scattered light shown in Fig. 4(b). To assist the discussion of the distribution of each phase, Fig. 4(c) shows the result of extracting and mapping the central wavenumber k_{220} of the 220 cm^{-1} peak obtained by the same fitting method as that shown in Fig. S1(a). The red and blue colors represent the high- and low-wavenumber sides, respectively. The wavenumber distribution before heating was almost uniform, indicating that the α-type, which is stable at room temperature, occupied most of the sample. However, there was also a part showing a high wavenumber of 224 cm^{-1}. When the sample was heated to 80 °C, the wavelength shifted slightly to the lower side and was distributed around an average value of 221.5 cm^{-1}. At 95 °C, where the β-type is the most stable phase, the wavenumber was distributed around 221 cm^{-1}. Thus, the wavenumber shifted to a lower value with increasing temperature.

On the other hand, when the sample was cooled from 120 °C, the sample was still in the liquid phase at 95 °C, and the wavenumber was distributed below 220 cm^{-1}. Upon further cooling, the wavenumber shifted to the higher-wavenumber side at 60 °C with the phase transition. An image with a different appearance from the scattered light and Raman intensity distributions appeared, indicating the importance of this high-resolution spectral analysis. Closer examinations revealed a mixture of a region with a wavenumber of about 222 cm^{-1}, which is often observed in the α-type phase, and a region with a high wavenumber of up to 224 cm^{-1}, as observed in Fig. 3(d). These results suggest that the sample was not a single uniform crystal. The region with the high wavenumber is considered to be the γ-type phase from the discussion of Fig. 4. It is considered that the γ-type phase did not immediately disappear even when the temperature was returned to room temperature, and the transition to the α-type phase took required an even longer time (see Fig. S7 for more detail). This method is highly expected to play an important role in the precise evaluation of materials, for example, bio-cells and lithium-ion batteries, in which S plays an important role.

In conclusion, we have developed a multi-plex CARS microscope that uses IR SC light as a light source. The separation of the signal and background is extremely important for low-wavenumber CARS. We have established a method of accurately distinguishing CARS signals. The developed system has potential for further refinement and is highly expected to advance the micro-characteristic evaluation of materials, for example, containing heavy atoms and polymers with low-wavenumber oscillations.

Acknowledgments We acknowledge the financial supports of a Grant-in-Aid for Scientific Research (17H06088, JP19H02591) from Japan Society for the Promotion of Science and Japan Core Research Evolutional Science and Technology (CREST) (JPMJCR1875).

Notes

The authors declare no competing interests.

1) C. V. Raman and K. S. Krishnan, Nature **121**, 501 (1928).
2) R. Loudon, Adv. Phys. **13**, 423 (1964).
3) R. G. Gordon, J. Chem. Phys. **43**, 1307 (1965).
4) F. Tuinstra and J. L. Koeing, J. Chem. Phys. **53**, 1126 (1970).
5) G. E. Walrafen, J. Chem. Phys. **40**, 3249 (1964).
6) H. Richter, Z. P. Wang, and L. Ley, Solid State Commun. **39**, 625 (1981).
7) M. Nuriya, H. Yoneyama, K. Takahashi, P. Leproux, V. Couderc, M. Yasui, and H. Kano, J. Phys. Chem. A **123**, 3928 (2019).
8) P. D. Maker and R. W. Terhune, Phys. Rev. **137**, A801 (1965).
9) A. Zumbusch, G. R. Holtom, and X. S. Xie, Phys. Rev. Lett. **82**, 4142 (1999).
10) J.-X. Cheng, A. Volkmer, and X. S. Xie, J. Opt. Soc. Am. B **19**, 1363 (2002).
11) K. Hashimoto, V. R. Badarla, A. Kawai, and T. Ideguchi, Nat. Commun. **10**, 4411 (2019).
12) L. Ren, I. Hurwitz, D. Raanan, P. Oulevey, D. Oron, and Y. Silberberg, Optica **6**, 52 (2019).
13) N. Dudovich, D. Oron, and Y. Silberberg, Nature **418**, 512 (2002).
14) H. Kano, T. Maruyama, J. Kano, Y. Oka, D. Kaneta, T. Guerenne, P. Leproux, V. Couderc, and M. Noguchi, OSA Continuum **2** , 1693 (2019).
15) H. Kano and H. Hamaguchi, Appl. Phys. Lett. **85**, 4298 (2004).

16) C. H. Camp Jr., Y. J. Lee, J. M. Heddleston, C. M. Hartshorn, A. R. H. Walker, J. N. Rich, J. D. Lathia, and M. T. Cicerone, Nat. Photonics **8**, 627 (2014).
17) C. Nims, B. Cron, M. Wetherington, J. Macalady, and J. Cosmidis, Sci. Rep. **9**, 7971 (2019).
18) S. Lebedkin, C. Blum, N. Stürzl, F. Hennrich, and M. M. Kappes, Rev. Sci. Instrum. **82**, 013705 (2011).
19) T. Barkhade, A. Phatangare, S. Dahiwale, S. K. Mahapatra, and I. Banerjee, Surf. Interface Anal. **51**, 894 (2019).
20) H. Xu, E. J. Bjerneld, M. Käll, and L. Börjesson, Phys. Rev. Lett. **83**, 4357 (1999).
21) H. Ito, H. Kurokawa, A. Hirayama, P. H. Indo, J. H. Majima, and H. Matsui, J. Clin. Biochem. Nutr. **61**, 183 (2017).
22) S. Venkatachalam, D. Bertin, G. Ducournau, J. F. Lampin, and D. Hourlier, Carbon **100**, 158 (2016).
23) J. T. Young, E. H. Tsai, and F. J. Boerio, Micromolecules **25**, 887 (1992).
24) P. Samyn, P. D. Baets, J. V. Craenenbroeck, F. Verpoort, and G. Schoukens, J. Appl. Polym. Sci. **101**, 1407 (2006).
25) Y. Yang, D. Yin, C. Zhong, R. Xiong, J. Shi, Z. Liu, X. Wang, and Q. Lei, Polym. Eng. Sci. **53**, 1536 (2013).